Wang *et al. Chem Synth* 2023;3:42
DOI: 10.20517/cs.2023.33

Chemical Synthesis

Research Article

Open Access

Check for updates

Revealing the dynamic formation mechanism of porous Mo_2C: an *in-situ* TEM study

Yongzhao Wang[1,2,#], Yiming Niu[1,2,#], Yinghui Pu[1,2], Shiyan Li[3], Yuefeng Liu[3], Bingsen Zhang[1,2,*]

[1]Shenyang National Laboratory for Materials Science, Institute of Metal Research, Chinese Academy of Sciences, Shenyang 110016, Liaoning, China.
[2]School of Materials Science and Engineering, University of Science and Technology of China, Shenyang 110016, Liaoning, China.
[3]Dalian National Laboratory for Clean Energy, Dalian Institute of Chemical Physics, Chinese Academy of Sciences, Dalian 116023, Liaoning, China.
[#]The authors contributed equally to this work.

[*]**Correspondence to:** Prof. Bingsen Zhang, Shenyang National Laboratory for Materials Science, Institute of Metal Research, Chinese Academy of Sciences, 72 Wenhua Road, Shenyang 110016, Liaoning, China. E-mail: bszhang@imr.ac.cn

How to cite this article: Wang Y, Niu Y, Pu Y, Li S, Liu Y, Zhang B. Revealing the dynamic formation mechanism of porous Mo_2C: an *in-situ* TEM study. *Chem Synth* 2023;3:42. https://dx.doi.org/10.20517/cs.2023.33

Received: 4 Jul 2023 **First Decision:** 28 Aug 2023 **Revised:** 11 Sep 2023 **Accepted:** 28 Sep 2023 **Published:** 10 Oct 2023

Academic Editors: Ying Wan, Jun Xu **Copy Editor:** Pei-Yun Wang **Production Editor:** Pei-Yun Wang

Abstract

In-situ transmission electron microscopy (TEM) enables direct observation of the micromorphology and microstructure evolution of catalysts in the chemical atmosphere. Studying the structural evolution during the formation of molybdenum carbide using *in-situ* TEM is helpful for the preparation of high-performance carbide catalysts. Herein, the formation mechanism of porous Mo_2C from MoO_2 nanoparticles (NPs) was studied by *in-situ* TEM. The formation of Mo_2C was induced by the defects of MoO_2, and the formed Mo_2C facilitated the carbonization of neighboring MoO_2 NPs. The growth rate of Mo_2C between MoO_2 NPs was slower compared to that within a single MoO_2 NP. In addition, the formation and growth of pores in Mo_2C were also studied; the pores grew radially during the early stages from the nucleation sites and later grew branched and curved. As Mo_2C underwent competitive growth, the pores transitioned from straight to curved. Eventually, during prolonged carbonization at high temperatures, Mo_2C underwent sintering.

Keywords: Mo_2C, porous structure, growth mechanism, *in-situ* TEM

INTRODUCTION

The transition metal carbides are widely used in industry due to their unique physical and chemical properties[1-7]. For instance, molybdenum (Mo) carbides can serve as supports in solid catalysts, which exhibit good performances in heterogeneous catalysis[8-10]. Moreover, Mo carbides also are the active phases, owning similar catalytic properties with the precious metals because of the introduction of carbon atoms[11-18]. They have been applied in hydrogenation[19-23], steam reforming of methanol[24], and water gas shift reaction[25]. Among them, β-Mo_2C demonstrated excellent activity and selectivity in CO_2 reduction[26], hydrogen production[27], and hydrodeoxygenation reactions[28]. Therefore, the research and development of preparation technology plays an important role in the application of high-performance Mo carbide catalysts. At present, the main preparation methods of Mo carbides include solid-solid and solid-gas (temperature-programmed reduction) reaction methods[29]. The solid-gas approach, which employs the reaction of the Mo oxides and the carbon-containing gases (e.g., CO, CH_4, C_2H_6, and aromatic compounds), was developed rapidly[30-36]. It is crucial to investigate the structural transformation process of Mo oxides into Mo carbides during temperature-programmed reduction carbonization.

Along with the development of preparation technologies for Mo carbides, the carbonization mechanism of Mo oxides to Mo carbides has also been studied intensively[37-39]. The carburization of MoO_3 with hydrocarbon and hydrogen was studied by the photoelectron spectroscopy[40]. The carbon deposition on the sample surface decreased with increasing carbon content. It indicated the diffusion of surface carbon on the sample into a bulk phase in the carburization process of Mo oxides. The MoO_2 was the intermediate phase determined by thermodynamic analysis in the process of MoO_3 transformed into Mo_2C[41]. Based on this, the structural evolution processes of MoO_2 in different carbon-containing gas atmospheres were investigated systematically. For example, the reduction of MoO_2 powders with CO to produce Mo_2C was studied, and the reduction mechanisms were significantly distinct at different temperatures[42]. The MoO_2 followed a one-step reaction translated to Mo_2C at lower temperatures. However, the transition process was different at high temperatures; the MoO_2 was reduced to Mo first, and then the Mo was carburized to Mo_2C. The transformation of MoO_2 to Mo_2C in a hydrocarbon atmosphere was also focused. The MoO_xC_y as the intermediate phases were observed during the carburization of MoO_2 in CH_4/H_2 or C_2H_6/H_2[43]. In addition, the mechanism of MoO_2 to Mo_2C under methane pulse conditions was also studied[44]. The researchers proposed the "plum-pudding" model in the solid-phase transformation from MoO_2 to Mo_2C. However, due to the limitation of characterization techniques, there are no relevant reports on the study of direct observation regarding Mo_2C formation processes in the preparation by temperature-programmed reduction methods. It seriously affects the perception and regulation of Mo_2C preparation. Usually, the direct reaction of Mo oxides with a carbon source at elevated temperatures generates β-Mo_2C. The investigation of their structural formation mechanism could provide guidance for the controllable preparation and also benefit the synthesis of Mo_2C with other phase structures.

In-situ transmission electron microscopy (TEM) has been used to directly visualize the structural evolution of nano-catalysts[45-47]. In recent years, the deoxidation process of MoO_3 was studied by environmental TEM, accompanied by the nanoparticles (NPs) crushing and regrowth in H_2 and thermal field, and the MoO_3 has a good directional deoxidation process[48]. Meanwhile, the different solid carbon sources were used, and the controllable growth of Mo carbides was monitored by *in-situ* TEM[49]. The face centered cubic (FCC) MoC with full occupation of interstitial sites by carbon sites was formed because the sucrose was decomposed into high reactivity sp^3 carbon atoms. The three-stage mechanism during nucleation and growth of Mo_2C NPs was also revealed by *in-situ* TEM[50]. Furthermore, if an atmosphere is introduced into TEM, the formation process of Mo carbides in the carbonation atmosphere can be directly observed. This helps to understand the mechanism of synthesizing Mo carbides by the solid-gas reaction method.

Herein, to get a better understanding of the formation mechanism of Mo oxides to Mo carbides in a temperature-programmed reduction method, we studied the microstructural evolutions of MoO_2 NPs to porous Mo_2C in a mixed atmosphere of methane and hydrogen by using *in-situ* TEM. And the mechanism of gas-solid reaction in the formation of Mo_2C was analyzed in detail.

EXPERIMENTAL

Synthesis of MoO_3 nanobelts

The typical solvothermal method applied to synthesize the MoO_3 nanobelts has been reported previously[51]. In brief, the 4,839 mg (0.02 mol) sodium molybdate dihydrate was dissolved in 60 mL deionized water after the 4 mL nitric acid was diluted by 16 mL deionized water and added to the stirred solution dropwise. Then, the solution was transferred into a 100 mL autoclave, sealed, and maintained at 130 °C for 12 h in an oven. Finally, the obtained deposition was filtered and washed with deionized water and then calcinated at 300 °C in air for 2 h. The MoO_2 was prepared by reducing MoO_3 nanobelts in H_2 or CH_4/H_2 atmosphere at 500 °C for 2 h with a heating rate of 10 °C/min. Mo_2C was synthesized under a CH_4/H_2 atmosphere at 700 °C for 2 h.

Samples characterization

TEM and high-angle annular dark field scanning TEM (HAADF-STEM) images were obtained using FEI Tecnai G^2 F20 operated at 200 kV. Scanning electron microscopy (SEM) images were obtained using Regulus 8100 operated at 3 kV. X-ray diffraction (XRD) measurements were performed on a Rigaku D/max 2400 diffractometer (Cu Kα radiation, λ = 0.15418 nm) operating at 40 kV and 40 mA. X-ray photoelectron spectroscopy (XPS) characterization was carried out with an ESCALAB 250 instrument with Al Kα X-rays (1,489.6 eV, 150 W, 50.0 eV pass energy). N_2 adsorption-desorption isotherms were measured on an ASAP 2020 micromeritics apparatus, and the specific surface areas of the samples were calculated following the multi-point BET (Brunauer-Emmett-Teller) procedure. The pore-size distributions were determined from the adsorption branch of the isotherms using the BJH (Barett-Joyner-Halenda) model.

CH_4/H_2 temperature programmed surface reaction (TPSR)

The 40 mg MoO_3 nanobelts were loaded in a quartz tube reactor that was connected to a mass spectrometer. Following, the samples were elevated to 700 °C with a heating rate of 5 °C/min under 20 vol.% CH_4/H_2 flow (5 mL/min). The mass signals of H_2 (Mz = 2) and H_2O (Mz = 18) were monitored during the process.

In-situ TEM investigation

The commercial gas-heating holder (produced by DENSsolutions), a home-made gas controlling system, and the Titan Themis G3 ETEM were adopted during the *in-situ* TEM experiments. The MoO_3 sample was encapsulated in a nanoreactor of a gas-heating holder. The nanoreactor has two amorphous SiN_x windows in order to observe the structural evolution of MoO_3 catalysts. The sample was calcinated at 300 °C in 20 vol.% O_2/He atmosphere for 30 min to remove any potential contamination before *in-situ* TEM experiments. Then, the temperature was lowered to room temperature, and the gas was switched to a 20 vol.% CH_4/H_2 atmosphere. The pressure in the nanoreactor was 1 bar during the test. Following, the temperature was sequentially elevated and kept at 500 °C, 600 °C, 700 °C, and 750 °C for *in situ* structural characterization.

RESULTS AND DISCUSSION

Characterization of the Mo oxides (carbides)

The typical XRD patterns and TEM images of MoO_3 nanobelts after calcination are shown in Supplementary Figure 1. The XRD pattern [Supplementary Figure 1A] confirmed the MoO_3 phase structure (JCPDS 65-2421) for MoO_3 nanobelts calcinated at 300 °C, and the sharp diffraction peaks verified the high

crystallinity. High-resolution TEM (HRTEM) with local fast Fourier transform (FFT) observation also identified the crystallographic property of MoO_3. The interplanar distances of 0.380 nm and 0.369 nm with an intersection angle of 90° were assigned to the (101) and (010) planes [Supplementary Figure 1C]. The sharp, bright diffraction spots are displayed in FFT [Supplementary Figure 1D], illustrating the high crystallinity of MoO_3 nanobelts, too. The temperature programmed surface reaction (TPSR) experiments show that the content change curves of H_2 and H_2O when MoO_3 nanobelts were reduced and carbonized [Supplementary Figure 2]. The reduction peaks at 500 °C and 600 °C indicate MoO_3 reduced to MoO_2 and MoO_2 transformed to Mo_2C, respectively. The second peak area of H_2O was larger than the first peak of H_2O, suggesting that there was a lot of water generated during the transformation from MoO_2 to Mo_2C. SEM images were used to show the morphology of MoO_2 and Mo_2C samples in Supplementary Figure 3. The produced MoO_2 by reducing MoO_3 nanobelts in the CH_4/H_2 atmosphere at 500 °C exhibited a plate-like shape. As the treatment temperature increased, the MoO_2 was carbonized to Mo_2C at 700 °C. The presence of porous agglomerates Mo_2C built up by MoO_2 platelets was observed. The MoO_2 and Mo_2C phases were confirmed by XRD [Supplementary Figure 3C and F] according to JCPDS 65-5787 and JCPDS 35-0787, respectively.

The STEM images and energy-dispersive X-ray spectroscopy (EDX) elemental maps of MoO_2 and Mo_2C samples were displayed in Supplementary Figure 4, exhibiting the well-distributed Mo/O in MoO_2 [Supplementary Figure 4A-C] and Mo/C in Mo_2C [Supplementary Figure 4D-F]. It indicated that the Mo oxides were completely transformed into the Mo carbides. TEM images and the EEL spectra of MoO_2 and Mo_2C samples [Supplementary Figure 5] show the morphology and electron structure changes of the samples before and after carbonization. It was observed that in plate-shaped MoO_2, there were Mo M-edges and O K-edges, while in porous Mo_2C, there were Mo M-edges and C K-edges, confirming the presence of pure phase structures of MoO_2 and Mo_2C. The XPS results were demonstrated and compared in Supplementary Figure 6. The peaks at 229.2 eV and 228.0 eV were assigned to Mo^{4+} and Mo^{2+}, respectively. As the MoO_2 transformed to Mo_2C, the content of Mo^{2+} species increased while the Mo^{4+} species highly decreased. The presence of Mo^{5+}(Mo^{6+}) species is ascribed to the surface oxidation while expositing to air.

Observation regarding the formation of porous Mo_2C

In order to understand the formation mechanism of Mo_2C, we observed the micromorphological and microstructural evolution of MoO_2 to Mo_2C at the nanoscale using *in-situ* TEM. Figure 1 exhibits the carbonization process of MoO_2 to Mo_2C under the 20 vol.% CH_4/H_2 atmosphere at ambient pressure. Figure 1A shows that the samples were MoO_2 NPs under the CH_4/H_2 atmosphere at 600 °C. The average particle size of MoO_2 NPs was 62.8 nm [Supplementary Figure 7]. When the temperature increased to 700 °C, the porous nanocrystals (pointed out with arrows) were observed, as shown in Figure 1B, suggesting the formation of Mo_2C at this temperature. Subsequently, the porous Mo_2C grew radially [Figure 1C]. As displayed in Figure 1D, most of MoO_2 NPs had been transformed into porous Mo_2C. Figure 1E shows the corresponding selected area electron diffraction (SAED) patterns of MoO_2 NPs [Figure 1A] and porous Mo_2C [Figure 1D] in the CH_4/H_2 atmosphere. The d-spacings of 3.42 Å, 2.43 Å, and 1.71 Å are close to the $d_{(011)}$, $d_{(020)}$, and $d_{(022)}$ referring to monoclinic MoO_2 (JCPDS 65-5787). Alternately, the d-spacings of 2.37 Å, 1.75 Å, and 1.30 Å are close to the $d_{(002)}$, $d_{(102)}$, and $d_{(200)}$ of hexagonal Mo_2C (JCPDS 35-0787). The diffraction spots transform into diffraction rings when MoO_2 is transformed into Mo_2C, indicating that the porous Mo_2C is polycrystalline. Figure 1F exhibits the intensity profiles from the integration of SAED patterns in Figure 1E, and it also confirmed the monoclinic MoO_2 and hexagonal Mo_2C pure phase structures for the samples in the CH_4/H_2 atmosphere at 600 and 700 °C, respectively. The unit cells [Figure 1G] and the histogram of cell volume and volume per Mo [Figure 1H] of MoO_2 and Mo_2C indicate that the formation of pores may be attributed to the volume reduction due to phase transformation, as there will be about 58.06% volume reduction when the same amount of Mo in the form of MoO_2 is converted to Mo_2C.

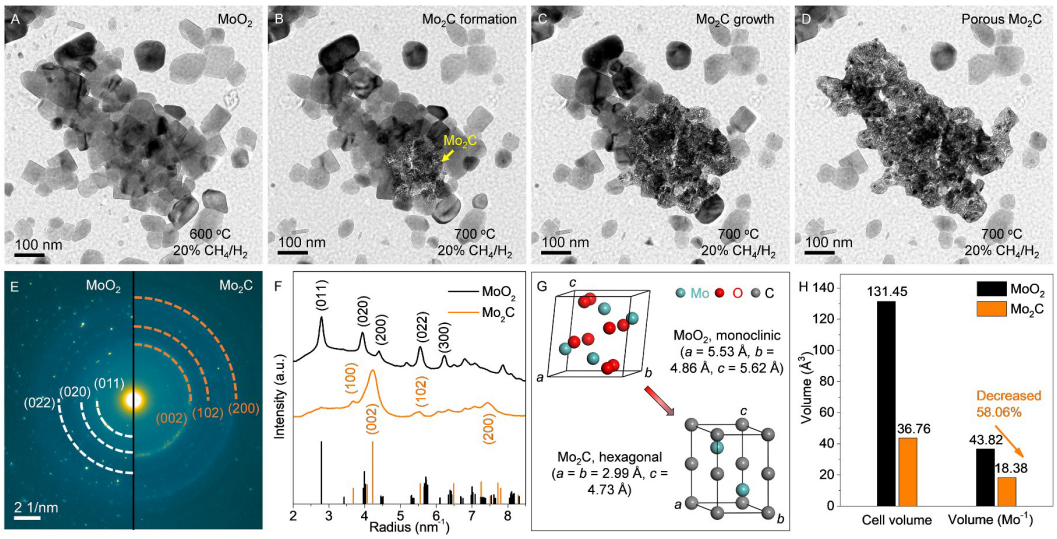

Figure 1. *In-situ* transformation from MoO_2 to Mo_2C. (A-D) *In-situ* TEM images of the Mo_2C formation from MoO_2 in 20 vol.% CH_4/H_2 atmosphere; (E) The corresponding SAED patterns of MoO_2 (A) and Mo_2C (D); (F) Intensity profiles from the integration of diffraction rings of SAED patterns in E (a.u., arbitrary units); (G) Unit cells of MoO_2 and Mo_2C; (H) The histogram of cell volume and volume per Mo of MoO_2 and Mo_2C. Mo: Molybdenum; SAED: selected area electron diffraction; TEM: transmission electron microscopy.

Unraveling the nucleation and growth of porous Mo_2C

Figure 2 displays the Mo_2C nucleation process of MoO_2 NPs under the drive of CH_4 and H_2 at 700 °C. Previous studies have illustrated that the methane was cracked into carbon with high reactivity at high temperatures, and the carbon species adsorbed on the surface of metal oxides[52,53]. In this experiment, the MoO_2 and highly reactive carbon further reacted and formed the Mo carbides. It is noteworthy that the defects in MoO_2 NPs were more likely to be carbonized preferentially. The preferential nucleation of Mo_2C was located at the defects of MoO_2 NPs. Figure 2F showed many small nanocrystals gradually appearing and the generation of pores at the defects of MoO_2 NPs, suggesting that the Mo_2C sites were formed here. Following, Mo_2C grew radially from the nucleation site in all directions at MoO_2 NPs [Figure 2H-J]. It proved that the defects in MoO_2 NPs induced the nucleation of Mo_2C. In addition, the carbonization process of two adjacent MoO_2 NPs was observed at 700 °C in the CH_4/H_2 atmosphere [Supplementary Figures 8 and 9]. Under the co-drive of CH_4 and H_2, the defects in MoO_2 NPs were carbonized first, and the NP transformed into porous Mo_2C. Subsequently, the carbonized MoO_2 NP induced the carbonization of adjacent MoO_2 NPs at the interface between two NPs. The carbonization reaction crossed the interface between two NPs and continued in the next MoO_2 NP. Lastly, the two MoO_2 NPs were turned to porous Mo_2C, and the grain boundary of the two NPs disappeared. It further reveals that the carbonization of MoO_2 NPs was also promoted by the adjacent already carbonized porous Mo_2C as the nucleating agents.

Generally, the MoO_2 NPs obtained by the reduction of MoO_3 nanobelts were usually stacked[54]. Herein, the growth rate of Mo_2C within and between MoO_2 NPs was studied [Figure 3]. There are approximately nine MoO_2 NPs stacked together in the observed two-dimensional (2D) region in Figure 3A. Figure 3K shows the growth rate of 2D area of porous Mo_2C in Supplementary Figure 10. The carbonization rate of MoO_2 NPs was represented by the growth rate of 2D area of porous Mo_2C. When Mo_2C grows across the interface between two MoO_2 NPs, it is considered to be carbonized between MoO_2 NPs. Alternately, when Mo_2C only grows inside MoO_2 NPs, it is carbonized within MoO_2 NPs. Judging from TEM images at 5 s, 10 s, and 15 s [Figure 3B-D], the carbonization reaction process between MoO_2 NPs was hindered and slowed down. This is mainly due to the presence of a high energy barrier at the grain boundary[55,56]. Compared with Figure 3D (15 s) and E (20 s), the Mo_2C growth rate within MoO_2 NPs

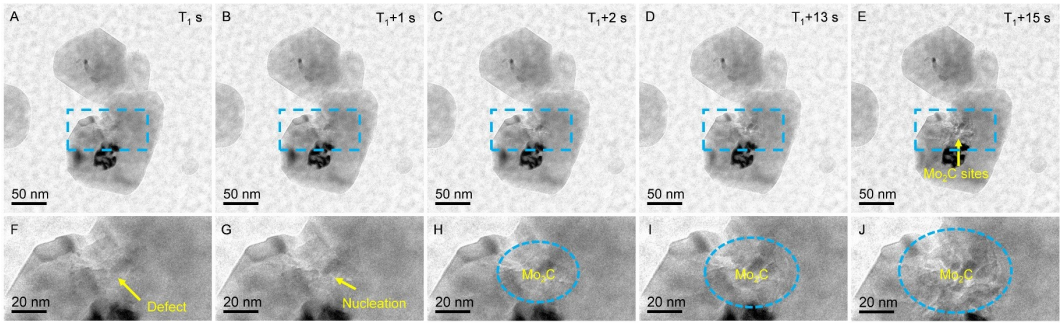

Figure 2. Defect-induced nucleation of Mo_2C. (A-E) *In-situ* TEM images of the nucleation process of Mo_2C under 20 vol.% CH_4/H_2 atmosphere at 700 °C; (F-J) Enlarged TEM images acquired from the dashed boxes in (A) to (E). TEM: Transmission electron microscopy.

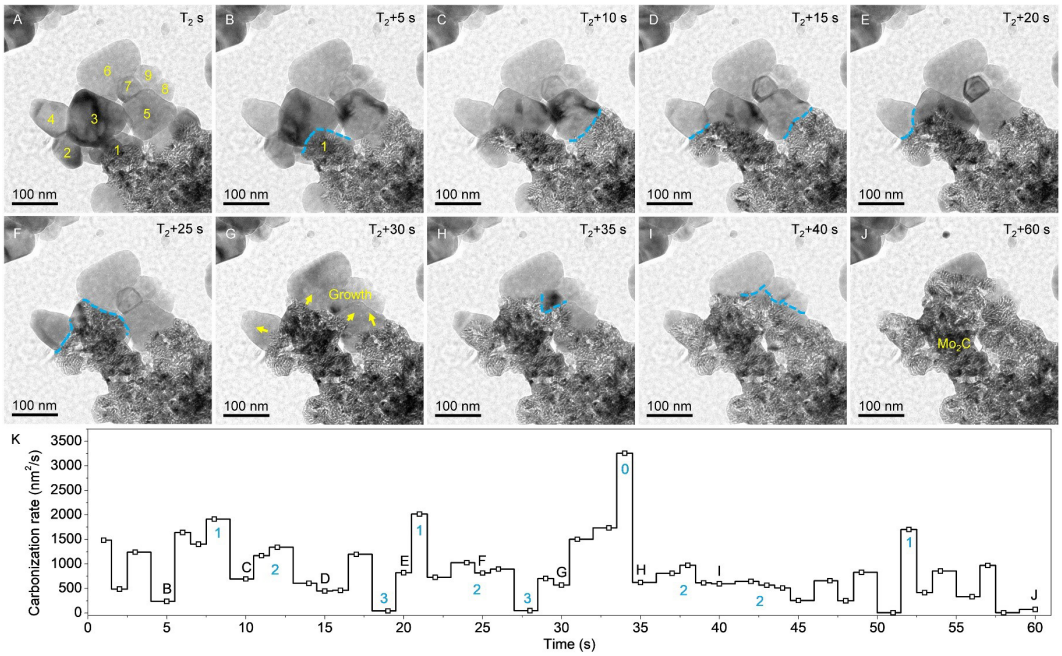

Figure 3. Growth rate of Mo_2C within and between MoO_2 NPs. (A-J) *In-situ* TEM images of structural evolution from stacked MoO_2 NPs to Mo_2C under 20 vol.% CH_4/H_2 atmosphere at 700 °C; (K) The carbonization rates within and between MoO_2 NPs. The boxes represent the growth rate of two-dimensional area of porous Mo_2C. Blue numbers represent the number of interfaces with Mo_2C growth crossing between MoO_2 NPs, and the capital letters represent the corresponding TEM images in (B-J). NPs: Nanoparticles; TEM: transmission electron microscopy.

increased after the carbonization reaction of MoO_2 crossed the interfaces between MoO_2 NPs. Especially from the 30 s [Figure 3F] to 35 s [Figure 3G], the growth of Mo_2C was quick, and the growth rate of 2D area of porous Mo_2C is over 3,000 nm^2/s. It was because of only the growth of Mo_2C within MoO_2 NPs during this period. After 35 s [Figure 3H-J], the growth of Mo_2C slowed down since Mo_2C growth crossed the interfaces between MoO_2 NPs and the reduction of Mo sources in a late stage of MoO_2 carbonization. Supplementary Figure 11 also exhibits that the growth rate of Mo_2C within MoO_2 NP was slower than that between MoO_2 NPs. The above results indicated that the presence of an interface between MoO_2 NPs could only slow down the carbonization process but not prevent it. After the carbonization reaction within and between MoO_2 NPs, the MoO_2 NPs were transformed into porous Mo_2C, and the interfaces between the original MoO_2 NPs disappeared.

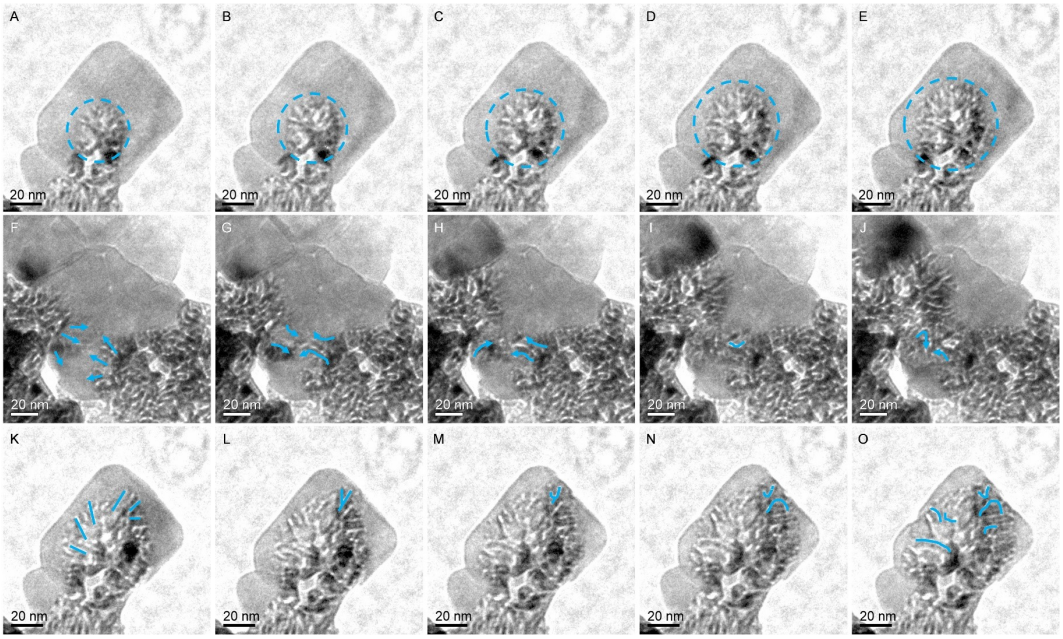

Figure 4. Growth types during the formation of Mo_2C. *In-situ* TEM images of radial (A-E), competition (B-J), and dendrite (K-O) growth of Mo_2C under 20 vol.% CH_4/H_2 atmosphere at 700 °C. TEM: Transmission electron microscopy.

Revealing the pore formation and evolution of porous Mo_2C

Subsequently, the formation of pores in the growth of Mo_2C was observed in Figure 4. The three types of porous Mo_2C growth were summarized. At the early stage, the pores showed radial growth from the center to the periphery [Figure 4A-E]. The structural transition from MoO_2 to Mo_2C was accompanied by the formation of straighter pores and faster pore growth rates. The competitive growth of pores was observed when two Mo_2C nucleation sites met during the carbonization process. As shown in Figure 4F-J, the straighter pores became distorted, and the growth rate of pores was slowed down during this process. In addition, the tip splitting and side branches of pores were observed in the late stage of growth. The growth of porous Mo_2C slowed down, and the pores curved due to the reduction of Mo sources [Figure 4K-O]. The above observations revealed that the growth and evolution of pores were affected by the amount of Mo sources. The pores of the Mo_2C radial grew and formed straighter pores when the Mo sources were sufficient. On the contrary, the pores of Mo_2C became curved and branched when the Mo sources were reduced.

Analyzing the microstructure of porous Mo_2C

Lastly, the micromorphology and structure of porous Mo_2C obtained by MoO_2 carbonization were analyzed, as shown in Figure 5. Figure 5B demonstrates the porous Mo_2C with different orientations of nanocrystals; the (101) facets with a lattice spacing of 2.29 Å were observed. The measured planes with lattice spacings of 2.61 Å, 2.29 Å, and 2.29 Å and angles of 64° and 52° in Figure 5C correspond to the crystal parameters of (010) 2.61 Å, (101) 2.29 Å and (1-11) 2.29 Å in hexagonal Mo_2C structures (JCPDS 35-0787). FFT pattern [Figure 5C] shows the hexagonal Mo_2C structure from the [-101] zone axis [Figure 5D]. The micromorphology and pore size of Mo_2C nanocrystal were computed in Supplementary Figure 12. The mean pore width and length are 1.4 nm and 9.7 nm, respectively. In addition, the N_2 physisorption tests [Supplementary Figure 13] were performed on MoO_2 and Mo_2C obtained after treatment at 600 and 700 °C, respectively. The low surface area of 1.11 $m^2 \cdot g^{-1}$ MoO_2 NPs translated to high surface area of 5.00 $m^2 \cdot g^{-1}$ porous Mo_2C. The pore-size distribution of MoO_2 showed a weak peak at 41.27 nm, whereas a strong peak at 2.21 nm was observed over porous Mo_2C, indicating that the pore formation in Mo_2C samples. However,

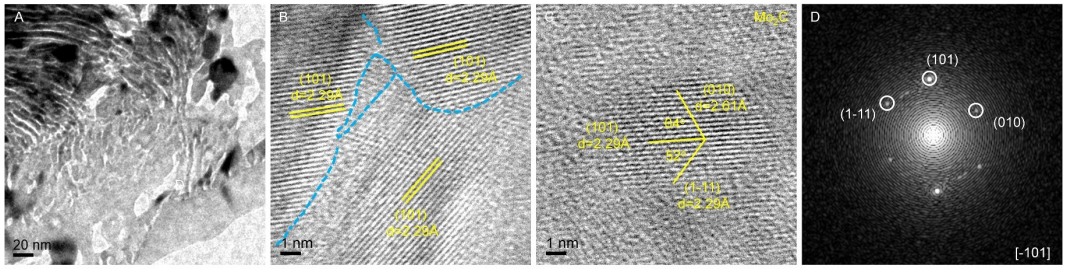

Figure 5. Characterization of the porous Mo_2C. *In-situ* TEM (A) and HRTEM (B and C) images of Mo_2C under 20 vol.% CH_4/H_2 atmosphere at 700 °C; (D) The corresponding FFT patterns of (C). FFT: Fast Fourier transform; HRTEM: high-resolution TEM; TEM: transmission electron microscopy.

the carbonization temperature of Mo_2C prepared by a temperature-programmed reduction method should not be too high. For example, Mo_2C samples undergo obvious sintering and disappearance of pores when the carbonization temperatures were increased to 750 °C from 700 °C, as shown in Supplementary Figure 14.

CONCLUSIONS

The structure evolution process of MoO_2 to porous Mo_2C in a carbonizing atmosphere was systemically investigated by using *in-situ* TEM. The formation of porous structures was observed during the carbonization process, which could be attributed to the volume decrease when an equivalent of Mo in the form of MoO_2 is converted to Mo_2C. The defects in MoO_2 NPs facilitated the nucleation of Mo_2C under CH_4/H_2 atmosphere at 700 °C. The porous Mo_2C induced the carbonization of neighboring MoO_2 NPs, and the interfaces between MoO_2 NPs slowed down the carbonization process. The carbonization reaction progressed from one MoO_2 NP to another through the interface. In the early growth stage of porous Mo_2C, the pores exhibited radial growth from the nucleation sites. However, in the late stage, the tip splitting and side branch formation of pores were observed. Moreover, the pores transitioned from straight to curved when the porous Mo_2C at different sites met during growth. Compared to MoO_2, the porous Mo_2C obtained through temperature-programmed reduction methods has a higher specific surface area. This work sheds light on the formation process of porous Mo_2C in a CH_4/H_2 atmosphere and could provide guidance for the synthesis of porous carbides.

DECLARATIONS

Authors' contributions

Design of the study and writing of the manuscript for the whole work: Wang Y, Niu Y, Zhang B
Performed the TEM characterization: Wang Y, Niu Y, Li S, Liu Y
Performed the analysis of data: Wang Y, Niu Y, Pu Y
Performed data acquisition and provided administrative, technical, and material support: Wang Y, Niu Y, Zhang B

Availability of data and materials

Experimental details on synthesis, characterization, and catalysis are available in the Supplementary Materials. Other raw data that support the findings of this study are available from the corresponding author upon reasonable request.

Financial support and sponsorship

This work was supported by the National Natural Science Foundation of China (Nos. 22072164, 22002173, 52161145403), the China Postdoctoral Science Foundation (2020M680999), the Natural Science Foundation of Liaoning Province (2022-MS-004), and the foundations of Shenyang National Laboratory for Materials Science.

Conflicts of interest

All authors declared that there are no conflicts of interest.

Ethical approval and consent to participate

Not applicable.

Consent for publication

Not applicable.

Copyright

REFERENCES

1. Lin Z, Denny SR, Chen JG. Transition metal carbides and nitrides as catalysts for thermochemical reactions. *J Catal* 2021;404:929-42. DOI
2. Li J, Chen X, Zhu X, Jiang Y, Chang X, Sun S. Two-dimensional transition metal MXene-based gas sensors: a review. *Chin Chem Lett* 2023:108286. DOI
3. Oyama S. Preparation and catalytic properties of transition metal carbides and nitrides. *Catal Today* 1992;15:179-200. DOI
4. Pang J, Sun J, Zheng M, Li H, Wang Y, Zhang T. Transition metal carbide catalysts for biomass conversion: a review. *Appl Catal B Environ* 2019;254:510-22. DOI
5. Dong S, Pu Y, Niu Y, Zhang L, Wang Y, Zhang B. Interstitial carbon in Ni enables high-efficiency hydrogenation of 1,3-butadiene. *Acta Phys Chim Sin* 2023;39:2301012. DOI
6. He K, Shen R, Hao L, et al. Advances in nanostructured silicon carbide photocatalysts. *Acta Phys Chim Sin* 2022;38:2201021. DOI
7. Du X, Zhang R, Li D, Hu C, Garcia H. Molybdenum carbide as catalyst in biomass derivatives conversion. *J Energy Chem* 2022;73:68-87. DOI
8. Yao S, Zhang X, Zhou W, et al. Atomic-layered Au clusters on α-MoC as catalysts for the low-temperature water-gas shift reaction. *Science* 2017;357:389-93. DOI
9. Dong J, Fu Q, Jiang Z, Mei B, Bao X. Carbide-supported Au catalysts for water-gas shift reactions: a new territory for the strong metal-support interaction effect. *J Am Chem Soc* 2018;140:13808-16. DOI PubMed
10. Lin L, Zhou W, Gao R, et al. Low-temperature hydrogen production from water and methanol using Pt/α-MoC catalysts. *Nature* 2017;544:80-3. DOI
11. Ma Y, Guan G, Hao X, Cao J, Abudula A. Molybdenum carbide as alternative catalyst for hydrogen production - a review. *Renew Sust Energ Rev* 2017;75:1101-29. DOI
12. Hou R, Chang K, Chen JG, Wang T. Replacing precious metals with carbide catalysts for hydrogenation reactions. *Top Catal* 2015;58:240-6. DOI
13. Frühberger B, Chen JG. Reaction of ethylene with clean and carbide-modified Mo(110): converting surface reactivities of molybdenum to Pt-group metals. *J Am Chem Soc* 1996;118:11599-609. DOI
14. Shi Y, Yang Y, Li Y, Jiao H. Activation mechanisms of H_2, O_2, H_2O, CO_2, CO, CH_4 and C_2H_x on metallic $Mo_2C(001)$ as well as Mo/C terminated $Mo_2C(101)$ from density functional theory computations. *Appl Catal A Gen* 2016;524:223-36. DOI
15. Du X, Liu J, Li D, et al. Structural and electronic effects boosting Ni-doped Mo_2C catalyst toward high-efficiency C-O/C-C bonds cleavage. *J Energ Chem* 2022;75:109-16. DOI
16. Wan C, Regmi YN, Leonard BM. Multiple phases of molybdenum carbide as electrocatalysts for the hydrogen evolution reaction. *Angew Chem Int Ed Engl* 2014;53:6407-10. DOI PubMed
17. Lian JH, Tan HY, Guo CQ, et al. Unravelling the role of ceria in improving the stability of Mo_2C- based catalysts for the steam reforming of dimethyl ether. *Catal Sci Technol* 2021;11:5570-8. DOI
18. Guo X, Wang C, Wang W, et al. Vacancy manipulating of molybdenum carbide MXenes to enhance Faraday reaction for high performance lithium-ion batteries. *Nano Res Energy* 2022;1:e9120026. DOI
19. Yang Q, Qiu R, Ma X, Hou R, Sun K. Surface reconstruction and the effect of Ni-modification on the selective hydrogenation of 1,3-butadiene over Mo_2C-based catalysts. *Catal Sci Technol* 2020;10:3670-80. DOI
20. Yue S, Xu D, Sheng Y, et al. One-step synthesis of mesoporous alumina-supported molybdenum carbide with enhanced activity for thiophene hydrodesulfurization. *J Environ Chem Eng* 2021;9:105693. DOI
21. Dongil AB, Zhang Q, Pastor-pérez L, Ramírez-reina T, Guerrero-ruiz A, Rodríguez-ramos I. Effect of Cu and Cs in the β-Mo_2C system for CO_2 hydrogenation to methanol. *Catalysts* 2020;10:1213. DOI
22. Rocha AS, Souza LA, Oliveira Jr RR, Rocha AB, da Silva VT. Hydrodeoxygenation of acrylic acid using Mo_2C/Al_2O_3. *Appl Catal A Gen* 2017;531:69-78. DOI
23. Ye X, Ma J, Yu W, et al. Construction of bifunctional single-atom catalysts on the optimized β-Mo_2C surface for highly selective

hydrogenation of CO_2 into ethanol. *J Energy Chem* 2022;67:184-92. DOI
24. Cao J, Ma Y, Guan G, et al. Reaction intermediate species during the steam reforming of methanol over metal modified molybdenum carbide catalysts. *Appl Catal B Environ* 2016;189:12-8. DOI
25. Wang G, Schaidle JA, Katz MB, Li Y, Pan X, Thompson LT. Alumina supported Pt-Mo_2C catalysts for the water-gas shift reaction. *J Catal* 2013;304:92-9. DOI
26. Zhang X, Liu Y, Zhang M, et al. Synergy between β-Mo_2C nanorods and non-thermal plasma for selective CO_2 reduction to CO. *Chem* 2020;6:3312-28. DOI
27. Ma FX, Wu HB, Xia BY, Xu CY, Lou XW. Hierarchical β-Mo_2C nanotubes organized by ultrathin nanosheets as a highly efficient electrocatalyst for hydrogen production. *Angew Chem Int Ed* 2015;54:15395-9. DOI
28. Murugappan K, Anderson EM, Teschner D, Jones TE, Skorupska K, Román-leshkov Y. Operando NAP-XPS unveils differences in MoO_3 and Mo_2C during hydrodeoxygenation. *Nat Catal* 2018;1:960-7. DOI
29. Vitale G, Guzmán H, Frauwallner ML, Scott CE, Pereira-almao P. Synthesis of nanocrystalline molybdenum carbide materials and their characterization. *Catal Today* 2015;250:123-33. DOI
30. Vitale G, Frauwallner M, Hernandez E, Scott C, Pereira-almao P. Low temperature synthesis of cubic molybdenum carbide catalysts via pressure induced crystallographic orientation of MoO_3 precursor. *Appl Catal A Gen* 2011;400:221-9. DOI
31. Chang H, Zhang G, Chou K. Topochemical synthesis of one-dimensional Mo_2C nanobelts. *Ceram Int* 2020;46:12891-6. DOI
32. Wang L, Zhang G, Chou K. Preparation of Mo_2C by reducing ultrafine spherical β-MoO_3 powders with CO or CO-CO_2 gases. *J Aust Ceram Soc* 2018;54:97-107. DOI
33. Li S, Kim WB, Lee JS. Effect of the reactive gas on the solid-state transformation of molybdenum trioxide to carbides and nitrides. *Chem Mater* 1998;10:1853-62. DOI
34. Xiao T, York APE, Coleman KS, et al. Effect of carburising agent on the structure of molybdenum carbides. *J Mater Chem* 2001;11:3094-8. DOI
35. Kugler EL, Clark CH, Wright JH, et al. Preparation, interconversion and characterization of nanometer-sized molybdenum carbide catalysts. *Top Catal* 2006;39:257-62. DOI
36. Jung KT, Kim WB, Rhee CH, Lee JS. Effects of transition metal addition on the solid-state transformation of molybdenum trioxide to molybdenum carbides. *Chem Mater* 2004;16:307-14. DOI
37. Alaba PA, Abbas A, Huang J, Daud WMAW. Molybdenum carbide nanoparticle: understanding the surface properties and reaction mechanism for energy production towards a sustainable future. *Renew Sust Energ Rev* 2018;91:287-300. DOI
38. Wang W, Han Y, Li Z, Liu X, Xu S. Phase equilibrium diagram and phase transformation for preparation of Mo_2C: thermodynamic study and experimental verification. *Ceram Int* 2020;46:755-62. DOI
39. Zhu L, Zhao Y, Yang W, Hsu H, Peng P, Li F. Low-temperature selective synthesis of metastable α-MoC with electrochemical properties: electrochemical co-reduction of CO_2 and MoO_3 in molten salts. *Chinese Chem Lett* 2023:108583. DOI
40. Koós Á, Oszkó A, Solymosi F. A photoelectron spectroscopic study of the carburization of MoO_3. *Appl Surf Sci* 2007;253:3022-8. DOI
41. Cetinkaya S, Eroglu S. Thermodynamic analysis and synthesis of porous Mo_2C sponge by vapor-phase condensation and in situ carburization of MoO_3. *J Alloys Compd* 2010;489:36-41. DOI
42. Dang J, Zhang G, Wang L, Chou K, Pistorius PC. Study on reduction of MoO_2 powders with CO to produce Mo_2C. *J Am Ceram Soc* 2016;99:819-24. DOI
43. Hanif A, Xiao T, York APE, Sloan J, Green MLH. Study on the structure and formation mechanism of molybdenum carbides. *Chem Mater* 2002;14:1009-15. DOI
44. Bkour Q, Cuba-torres CM, Marin-flores OG, et al. Mechanistic study of the reduction of MoO_2 to Mo_2C under methane pulse conditions. *J Mater Sci* 2018;53:12816-27. DOI
45. Wang Y, Niu Y, Gao T, Liu S, Zhang B. Assessing the effect of the electron-beam irradiation on Pd/Ga_2O_3 catalyst under ambient pressure. *ChemCatChem* 2020;12:4765-9. DOI
46. Niu Y, Liu X, Wang Y, et al. Visualizing formation of intermetallic PdZn in a palladium/zinc oxide catalyst: interfacial fertilization by PdH_x. *Angew Chem Int Ed Engl* 2019;58:4232-7. DOI
47. Li C, Liu B, Jiang N, Ding Y. Elucidating the charge-transfer and Li-ion-migration mechanisms in commercial lithium-ion batteries with advanced electron microscopy. *Nano Res Energy* 2022;1:e9120031. DOI
48. Ma P, Li A, Wang L, Zheng K. Investigation of deoxidation process of MoO_3 using environmental TEM. *Materials* 2021;15:56. DOI PubMed PMC
49. Lin Z, Cai L, Lu W, Chai Y. Phase and facet control of molybdenum carbide nanosheet observed by in situ TEM. *Small* 2017;13:1700051. DOI PubMed
50. Fei L, Ng SM, Lu W, et al. Atomic-scale mechanism on nucleation and growth of Mo_2C nanoparticles revealed by in situ transmission electron microscopy. *Nano Lett* 2016;16:7875-81. DOI
51. Yang S, Wang Z, Hu Y, et al. Highly responsive room-temperature hydrogen sensing of α-MoO_3 nanoribbon membranes. *ACS Appl Mater Interfaces* 2015;7:9247-53. DOI
52. Bonnet F, Ropital F, Berthier Y, Marcus P. Filamentous carbon formation caused by catalytic metal particles from iron oxide. *Mater Corros* 2003;54:870-80. DOI
53. Zou Z, Fu L, Song X, Zhang Y, Liu Z. Carbide-forming groups IVB-VIB metals: a new territory in the periodic table for CVD growth

of graphene. *Nano Lett* 2014;14:3832-9. DOI

54. Hu B, Mai L, Chen W, Yang F. From MoO_3 nanobelts to MoO_2 nanorods: structure transformation and electrical transport. *ACS Nano* 2009;3:478-82. DOI
55. Guo X, Maier J. Grain boundary blocking effect in zirconia: a schottky barrier analysis. *J Electrochem Soc* 2001;148:E121. DOI
56. Rohrer GS. The role of grain boundary energy in grain boundary complexion transitions. *Curr Opin Solid St M* 2016;20:231-9. DOI